Transactions on Energy Systems and Engineering Applications

Article

MHD hybrid nanofluid flow and entropy analysis in smooth and wavy channels under non-uniform magnetic field

Souad Benkherbache[1], Salah Amroune[1], Firas F. Qader[2], Rawand Sardar Abdulrahman[3] and Barhm Mohamad[3,*]

[1] Laboratory of Materials and Mechanics of Structures (LMMS), Faculty of Technology, University of M'sila, PO. Box. 166 Ichebilia 28000 M'sila, Algeria.
[2] Kirkuk Technical Engineering College, Northern Technical University, Kirkuk 36001, Iraq.
[3] Department of Petroleum Technology, Koya Technical Institute, Erbil Polytechnic University, 44001 Erbil, Iraq.
[*] Correspondence:

Received: 04 April 2026; Accepted: 17 June 2026; Published: 18 August 2026

Abstract: This study presents a comprehensive numerical investigation of magneto hydrodynamic (MHD) hybrid nanofluid flow in a two-dimensional channel featuring a localized wavy section under the influence of a non-uniform magnetic field. The hybrid nanofluid, composed of Fe_3O_4–Al_2O_3 nanoparticles dispersed in water, is modeled as a single-phase fluid under laminar, steady, and incompressible conditions. The applied transverse magnetic field follows an exponential decay along the channel height, inducing a spatially varying Lorentz force and Joule heating effect. The governing equations are solved using the finite volume method implemented in ANSYS Fluent, with the SIMPLE algorithm employed for pressure–velocity coupling. A comparative analysis between smooth (SC) and wavy (WC) channel configurations is conducted to evaluate the impact of Reynolds number ($200 \leq Re \leq 800$) and magnetic field intensity ($1\ T \leq B_0 \leq 8\ T$) on flow structure, heat transfer, and thermodynamic irreversibility. The results reveal that the magnetic field significantly suppresses fluid velocity within the magnetized region due to Lorentz force damping, while simultaneously enhancing fluid temperature through Joule heating. Overall, the results demonstrate that the combination of localized wall waviness and a non-uniform magnetic field provides an effective strategy for enhancing heat transfer while minimizing thermodynamic irreversibility. This study offers valuable insights for the design of advanced MHD-based cooling systems and energy applications involving hybrid nanofluids.

 https://doi.org/10.32397/tesea.vol7.n2.1011

How to cite this article: Benkherbache, Souad; Amroune, Salah; Qader, Firas F.; Abdulrahman, Rawand Sardar; Mohamad, Barhm. MHD hybrid nanofluid flow and entropy analysis in smooth and wavy channels under non-uniform magnetic field. *Transactions on Energy Systems and Engineering Applications*, 7(2): 1011, 2026. DOI:10.32397/tesea.vol7.n2.1011

1. Introduction

Nanofluids are precisely engineered mixtures created by dispersing nanoscale solid particles (such as metals, metal oxides, or carbon-based materials) into conventional base fluids like water, oil, or ethylene glycol. Their primary purpose is to enhance the thermal and physical properties of the base fluid, particularly its thermal conductivity [1–3]. This made them highly valuable for various heat transfer applications, including electronics cooling, automotive engines and industrial processes [4]. Recent advances in this field have also explored their potential in more complex systems involving magnetic fields and porous media [5,6]. Building on this foundation, recent research has shifted focus toward hybrid nanofluids, which combine two or more different types of nanoparticles to achieve even superior thermophysical properties and synergistic effects. According to Suresh et al. [7] hybrid nanofluids have become a cornerstone of modern thermal investigations due to their enhanced thermophysical properties and superior heat transfer capabilities over standard nanofluids. is a fundamental area of study for cooling systems and microelectronic devices. Arshad et al. [8] examined rotating flows incorporating chemical reactions and radiation, finding that oxide-based hybrids outperform mixed nanoparticle suspensions. Further investigations by Xu [9] and Roy & Pop [10] highlighted that hybrid suspensions effectively delay flow reversal and that higher concentrations can improve heat transfer by up to 21% at the walls. Comprehensive reviews by Sarkar et al. [11] and Huminic & Huminic [12] emphasize that hybridization aims to balance heat transfer gains with pressure drop characteristics, despite ongoing challenges regarding stability.

Recent numerical investigations have focused on the flow dynamics of these fluids in specific geometries. For instance, Shaheen et al. [13] demonstrated the strong influence of the Reynolds and magnetic parameters on velocity gradients. Benkherbache et al. [14] showed that while geometric features like fins can enhance performance in some cavities, they may also inhibit convection if not properly optimized. Similarly, Waini et al. [15] utilized stability analysis to confirm the consistency of dual solutions in stretching/shrinking sheet problems. These studies collectively highlight that hybrid nanofluids outperform mono-nanofluids, making them critical for advanced cooling processes in aviation and industrial engineering.

The thermal behavior of hybrid nanofluids under magneto hydrodynamic (MHD) conditions has been extensively explored using various numerical techniques. For instance, Albqmi & Sivanandam [16] utilized the bvp4c method to examine the impact of thermal radiation and entropy generation on Al_2O_3/H_2O flow, while Ali et al. [17] employed the Successive-Over-Relaxation (SOR) technique to simulate hybrid $Cu-Al_2O_3/H_2O$ flow in porous media, noting significant increases in shear stress. The advancement of meshless methods has also contributed to this field; Tayari et al. [18] and Hosseinzadeh & Ganji [19] implementing Radial Basis Functions RBF to investigate the effects of Brownian motion and shape factors on hybrid mixtures between parallel plates. Furthermore, the complexity of these systems has been increased by considering ternary mixtures and biological effects; Anwar et al. [20] revealed that integrating Joule heating and thermal radiation in ternary hybrid nanofluids can enhance the Nusselt number by over 13%. To refine flow control, researchers have explored diverse geometries and constraints. Ali et al. [21] proposed the use of a Riga plate to induce wall-parallel Lorentz forces, while other works have investigated non-linear couple stress , irregular or wavy channels , and unsteady turbulent flows. Additionally, the use of the Lattice Boltzmann Method LBM and sensitivity analyses in trapezoidal or wavy cavities confirm that the synergy between geometric undulations and magnetic orientation is essential for optimizing heat transfer rates.

Other investigations have focused on diverse geometries and additional physical constraints to broaden the understanding of magneto-convective transport. Recent works have explored the impact of non-linear couple stress in ternary mixtures, shape factor effects between parallel plates using RBF methods, and the behavior of hybrid fluids in irregular or wavy channels [22–24]. Specifically, studies on Fe_3O_4-based hybrids along vertical wavy surfaces and unsteady turbulent flows over movable wedges have shown that the magnetic parameter significantly modulates the thermal and solutal boundary layers. Additionally, the use of the Lattice Boltzmann Method LBM in channels with active heaters and sensitivity analyses in trapezoidal or wavy cavities confirm that the synergy between geometric undulations and magnetic orientation is key to optimizing heat transfer rates [25–29].

Beyond the primary analysis of heat transfer enhancement, the evaluation of thermodynamic efficiency through the Second Law of Thermodynamics has become a pivotal aspect of modern fluid dynamics. Tlau and Ontela [30] investigated entropy generation in MHD nanofluid flows identifying that production reaches its minimum just above the channel center. In the context of hybrid nanofluids, Parveen et al. [31] and Ahmad et al. [32] demonstrated that while hybridization with particles like Fe_3O_4 and Ag significantly boosts thermal conductivity, they also alter irreversibility distributions where magnetic induction and variable thermal controls play a decisive role.

The impact of magnetic fields on these irreversibilities is further complicated by Joule heating and viscous dissipation. Tahiri et al. [33] and Nadeem et al. [34] highlighted that maximum entropy generation typically occurs near the channel walls, especially under high Hartmann numbers and intense radiative-convective conditions. For flows in porous media, Jena & Mishra [35] performed a comparative study revealing that Cu-Al_2O_3 hybrid nanofluids often exhibit lower entropy generation compared to their mono-nanofluid counterparts, a finding supported by Hussain et al. [36] over stretching surfaces.

Recent investigations have focused on optimizing these thermal systems within complex enclosures. Abdulkadhim et al. [37] and Bilal et al. [38] explored corrugated and star-shaped enclosures, finding that while longer corrugated lengths improve heat transfer but often increase total entropy, necessitating a careful analysis of the Bejan number to balance thermal and friction losses. Notably, Mehrali et al. [39] and Mabood et al. [40] demonstrated that the use of magnetic hybrid nanofluids can reduce the total entropy generation rate by up to 41%. Furthermore, studies [41, 42] on shrinking sheets and rotating channels confirm that the magnetic parameter and high Biot numbers are primary drivers in minimizing thermal irreversibility.

Despite these comprehensive studies on various geometries like cavities [24, 43] and Riga plates [21]. The specific interaction between a localized wavy section and an exponentially decaying magnetic field regarding the volumetric distribution of the Bejan number has not yet been addressed. This research gap is particularly relevant for the Fe_3O_4-Al_2O_3/H_2O hybrid mixture, where magnetic responsiveness and geometric undulations can be strategically combined to achieve entropy optimization.

While the aforementioned studies have laid a solid foundation for understanding magneto-convective transport and irreversibility in hybrid systems, a specific gap remains regarding the localized control of heat transfer in complex geometries. Most existing literature focuses on either uniform magnetic fields or fully corrugated channels. However, no study has combined the effect of an exponentially decaying magnetic field with a partially wavy channel section containing a Fe_3O_4-Al_2O_3/H_2O hybrid nanofluid. Understanding how this localized geometric perturbation interacts with a spatially varying Lorentz force is crucial for the design of targeted cooling systems where thermal management is only required in specific zones. This research gap necessitates a comprehensive investigation of the thermal behavior of hybrid nanofluids under magnetohydrodynamic conditions using advanced numerical techniques.

The present study aims to fill this gap by conducting a comprehensive numerical investigation of the thermo-hydraulic behavior and entropy generation in this configuration. The specific objectives are as follows:

- To evaluate the impact of the Reynolds number and magnetic field intensity on the flow structure and temperature distribution within the wavy section.
- To conduct a comparative analysis between the Smooth Channel (SC) and the Wavy Channel (WC) configurations to quantify the heat transfer augmentation Nu.

- To perform a detailed thermodynamic optimization by calculating the volumetric entropy generation and the local Bejan number.
- To identify the best balance between heat transfer enhancement and entropy generation under a non-uniform magnetic field.

2. Physical Model

The physical system investigated in this study is a two-dimensional microchannel of height $H = 0.01$ m and total length $L = L_1 + L_2 + L_3 = 0.7$ m, as illustrated in Figure 1. The channel is divided into three distinct longitudinal sections: an inlet section ($L_1 = 0.4$ m), a central active section ($L_2 = 0.2$ m), and an outlet section ($L_3 = 0.1$ m).

To assess the impact of geometric perturbations on the thermal performance, two configurations are compared: a Smooth Channel (SC) and a Wavy Channel (WC). In the WC configuration, the central section (L_2) features a localized corrugated profile. Based on the coordinate system with the origin (0,0) at the lower inlet corner, the upper and lower wall profiles for $x_s \leq x \leq x_s + L_2$ are defined as:

$$y_{Lower}(x) = A \sin\left(\frac{2\pi}{\lambda}(x - x_s)\right), \tag{1}$$

$$y_{Upper}(x) = H - A \sin\left(\frac{2\pi}{\lambda}(x - x_s)\right), \tag{2}$$

where A represents the amplitude of the wall waviness, λ is the wavelength of the sinusoidal profile, and x_s denotes the starting location of the wavy section.

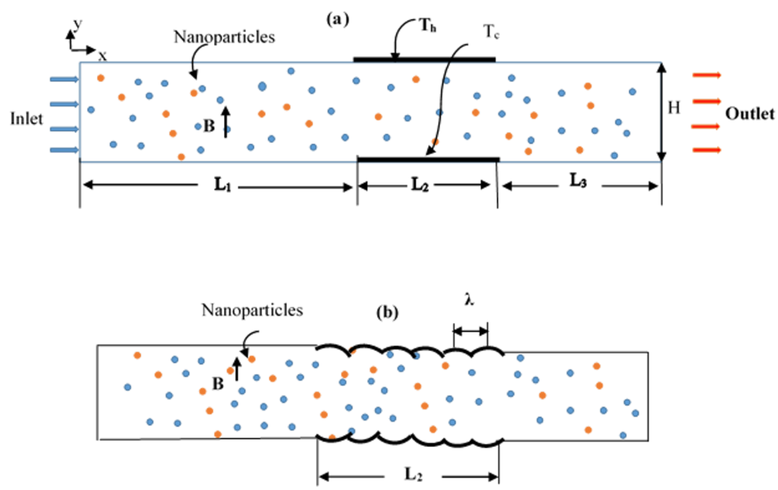

Figure 1. Schematic representation of the computational domain for the two channel configurations: (a) smooth channel (SC) and (b) wavy channel (WC).

The channel is filled with a Fe_3O_4-Al_2O_3/water hybrid nanofluid, assumed to be steady, laminar, and incompressible. The nanoparticles and the base fluid are considered to be in local thermal equilibrium and moving with the same velocity. The fluid enters the domain with a uniform velocity and a cold temperature $T_0 = 298$ K. Regarding the thermal boundary conditions, the central active walls are maintained at high temperatures: $T_h = 380$ K for the upper plate and $T_c = 350$ K for the lower plate, while the remaining boundary sections are kept at 300 K. At the outlet, fully developed flow conditions are imposed. The thermophysical properties of the base fluid and the nanoparticles are summarized in Table 1 [44].

Table 1. Thermophysical properties of pure water and Fe_3O_4 and Al_2O_3 nanoparticles [44].

Material	ρ **(kg/m³)**	k **(W/mK)**	C_p **(J/kgK)**	σ **(S/m)**	β **(1/K)**
Water	998	0.608	4182	0.05	2.1×10^{-4}
Fe_3O_4	5180	6	670	2.5×10^4	1.3×10^{-5}
Al_2O_3	3970	40	765	1×10^{-10}	0.85×10^{-5}

A non-uniform transverse magnetic field is applied perpendicular to the flow direction. Unlike standard longitudinal variations, the intensity of this field decays exponentially along the transverse (y) direction, following the relation $B(y) = B_0 e^{-ky}$. This configuration induces a variable Lorentz force across the channel height, which, combined with the Joule heating and the Boussinesq approximation for buoyancy, governs the MHD behavior of the hybrid nanofluid. The effective properties of the mixture are evaluated using the models listed in Table 2 [45].

Table 2. Thermophysical characteristics of hybrid nanofluid [45].

Property	**Model**
Density	$\rho_{hnf} = (1-\varphi)\rho_f + \varphi_1\rho_1 + \varphi_2\rho_2$
Heat capacitance	$(\rho C_p)_{hnf} = (1-\varphi)(\rho C_p)_f + \varphi_1(\rho C_{p1}) + \varphi_2(\rho C_{p2})$
Thermal expansion	$(\rho\beta)_{hnf} = (1-\varphi)(\rho\beta)_f + \varphi_1(\rho\beta_1) + \varphi_2(\rho\beta_2)$
Electrical conductivity	$\frac{\sigma_{hnf}}{\sigma_f} = 1 + \frac{3\left[\frac{(\varphi_1\sigma_1+\varphi_2\sigma_2)}{\sigma_f} - (\varphi_1+\varphi_2)\right]}{\left(\frac{(\varphi_1\sigma_1+\varphi_2\sigma_2)}{\varphi\sigma_f} + 2\right) - \left(\frac{(\varphi_1\sigma_1+\varphi_2\sigma_2)}{\sigma_f} - (\varphi_1+\varphi_2)\right)}$
Thermal conductivity	$\frac{k_{hnf}}{k_f} = 1 + \frac{\left[\frac{(\varphi_1 k_1+\varphi_2 k_2)}{\varphi} + 2k_f + 2(\varphi_1 k_1+\varphi_2 k_2) - 2\varphi k_f\right]}{\left(\frac{(\varphi_1 k_1+\varphi_2 k_2)}{\varphi} + 2k_f\right) - \left((\varphi_1 k_1+\varphi_2 k_2) + \varphi k_f\right)}$
Thermal diffusivity	$\alpha_{hnf} = \frac{k_{hnf}}{(\rho C_p)_{hnf}}$
Dynamic viscosity	$\mu_{hnf} = \frac{\mu_f}{(1-(\varphi_1+\varphi_2))^{2.5}}$

3. Governing Equations

To describe the two-dimensional, steady, laminar, and incompressible MHD flow of the Fe_3O_4-Al_2O_3/water hybrid nanofluid, the following assumptions are adopted. The mixture is considered to be in a state of local thermal equilibrium, behaving as a single-phase homogeneous fluid with negligible velocity slip between the phases. Due to the low magnetic Reynolds number, the induced magnetic field is neglected in comparison to the externally applied exponential field $B(y)$. Furthermore, the Boussinesq approximation is employed to account for buoyancy effects. Under these considerations, the conservation equations for mass, momentum, and energy are formulated as follows:

Continuity equation

$$\rho_{hnf}\left(\frac{\partial u}{\partial x}+\frac{\partial v}{\partial y}\right)=0. \tag{3}$$

Momentum equations

$$\rho_{hnf}\left(u\frac{\partial u}{\partial x}+v\frac{\partial u}{\partial y}\right)=-\frac{\partial p}{\partial x}+\mu_{hnf}\left(\frac{\partial^2 u}{\partial x^2}+\frac{\partial^2 u}{\partial y^2}\right)-\sigma_{hnf}B^2(y)\,u, \tag{4}$$

$$\rho_{hnf}\left(u\frac{\partial v}{\partial x}+v\frac{\partial v}{\partial y}\right)=-\frac{\partial p}{\partial y}+\mu_{hnf}\left(\frac{\partial^2 v}{\partial x^2}+\frac{\partial^2 v}{\partial y^2}\right)-\rho_{hnf}\,g\,\beta_{hnf}(T-T_0). \tag{5}$$

Energy equation

$$\rho_{hnf}\left(u\frac{\partial T}{\partial x}+v\frac{\partial T}{\partial y}\right)=\frac{k_{hnf}}{(C_p)_{hnf}}\left(\frac{\partial^2 T}{\partial x^2}+\frac{\partial^2 T}{\partial y^2}\right)+\sigma_{hnf}B^2(y)\,u^2. \tag{6}$$

The last terms in Equations (4) to (6) represent the Lorentz force, the buoyancy force, and the magnetic Joule heating, respectively. The corresponding boundary conditions applied in the present model are listed in Table 3.

Table 3. Boundary conditions of the present model.

Axial section	**Boundary**	**Velocity condition**	**Temperature conditions and magnetic field**
Section I	L_1, $0 \le x \le 0.4$ m	$u=0, v=0$	Upper plate: $T=300$ K, Lower plate: $T=300$ K
Section II (SC)	L_2, $0.4 < x \le 0.6$ m	$u=0, v=0$	Upper plate: $T_h=380$ K, Lower plate: $T_c=350$ K, $B=B_0e^{-Ky}$
Section II (WC)	L_2, $0.4 < x \le 0.6$ m	$y_{Upper}(x) = H - A\sin\left(\frac{2\pi}{\lambda}(x-x_s)\right)$, $y_{Lower}(x)=A\sin\left(\frac{2\pi}{\lambda}(x-x_s)\right)$, $u=0$, $v=0$	$T_h=380$ K, $T_c=350$ K, $B=B_0e^{-Ky}$
Section III	L_3, $0.6 < x \le 0.7$ m	$u=0, v=0$	Upper plate: $T=300$ K, Lower plate: $T=300$ K
Inlet	$x=0$, $0<y\le 0.01$ m	$u=u_0, v=0$	$T=298$ K
Outlet	$x=0.7$ m, $0<y\le 0.01$ m	$\partial u/\partial x=0, v=0$	$\partial T/\partial x=0$

3.1. Dimensionless parameters

The thermo-hydraulic behavior of the current hybrid MHD nanofluid system is fundamentally determined by the dimensionless Reynolds, Rayleigh, Hartmann, and Prandtl numbers.

The Reynolds number: $Re = \dfrac{\rho_{hnf} V D_h}{\mu_{hnf}}$.
The Rayleigh number: $Ra = \dfrac{g\,\beta_{hnf}(T_h - T_c)H^3}{\nu_{hnf}\,\alpha_{hnf}}$.
The Prandtl number: $Pr = \dfrac{\mu_{hnf}}{\alpha_{hnf}}$.
The Hartmann number: $Ha(y) = H\,B(y)\sqrt{\dfrac{\sigma_{hnf}}{\mu_{hnf}}}$.

3.2. Heat transfer and Nusselt number

The local Nusselt number along the heated upper wall is defined based on the hydraulic diameter as:

$$Nu(x) = \frac{h(x)\,D_h}{k_{hnf}}, \tag{7}$$

$h(x)$ is convective heat transfer coefficient and defined by the following:

$$h(x) = \frac{q(x)}{T_w - T_b}, \tag{8}$$

$q(x)$ is the local heat flux, T_w and T_b are respectively the wall and the bulk fluid temperature. T_b is calculated as follows:

$$T_b = \frac{\iint u\,T\,dx\,dy}{\iint u\,dx\,dy}. \tag{9}$$

The average Nusselt number is obtained by integrating the local values over the heated section of L_2:

$$Nu_{avg} = \frac{1}{L_2}\int_{x_1}^{x_2} Nu(x)\,dx = \frac{h(x)\,D_h}{k_{hnf}} = \frac{q(x)\,D_h}{k_{hnf}(T_w - T_b)}. \tag{10}$$

3.3. Magnetic field distribution

The non-uniform transverse magnetic field intensity varies exponentially along the transverse direction according to

$$B(y) = B_0\,e^{-ky}, \tag{11}$$

where B_0 denotes the reference magnetic field strength, and k is the magnetic decay coefficient.

Lorentz force

The influence of the non-uniform magnetic field on the hybrid nanofluid flow is analyzed through the Lorentz force and the magnetic Joule heating terms. The induced electric current **j** and the Lorentz force F_L are defined as:

$$\vec{j} = \sigma(\vec{V} \times \vec{B}), \tag{12}$$

and,

$$F_L = \vec{j} \times \vec{B} \Rightarrow F_L = \sigma_{hnf} B^2(y)\,u. \tag{13}$$

In the present configuration, the Lorentz force acts opposite to the main flow direction and produces a magnetic damping effect, which reduces the fluid velocity. This magnetic braking mechanism becomes stronger as the magnetic field intensity increases.

Magnetic Joule heating

The magnetic field also introduces a volumetric heat generation term, known as magnetic Joule heating, defined as:

$$Q_j = \sigma_{hnf} B^2(y)\, u^2 \tag{14}$$

This term is incorporated into the energy equation and contributes to the increase in fluid temperature, especially in regions of high velocity and strong magnetic field intensity.

3.4. Entropy generation analysis

We use the entropy generation analysis to evaluate the thermodynamic irreversibility associated with heat transfer, fluid friction, and magnetic effects in the hybrid nanofluid flow. The total local entropy generation rate is expressed as the sum of thermal, viscous, and magnetic contributions [46]:

$$S_{tot} = S_{th} + S_{vis} + S_{mag}. \tag{15}$$

Thermal entropy generation

The entropy generation due to heat transfer is given by:

$$S_{th} = \frac{k_{hnf}}{T^2}\left[\left(\frac{\partial T}{\partial x}\right)^2 + \left(\frac{\partial T}{\partial y}\right)^2\right]. \tag{16}$$

It represents the irreversibility associated with temperature gradients inside the flow domain.

Viscous entropy generation

The entropy generation due to fluid friction is expressed as:

$$S_{vis} = \frac{\mu_{hnf}}{T}\left[2\left(\frac{\partial u}{\partial x}\right)^2 + 2\left(\frac{\partial v}{\partial y}\right)^2 + \left(\frac{\partial u}{\partial y} + \frac{\partial v}{\partial x}\right)^2\right]. \tag{17}$$

It accounts for the energy dissipation caused by velocity gradients.

Magnetic entropy generation

The entropy generation associated with magnetic effects is defined as:

$$S_{mag} = \frac{\sigma_{hnf} B^2(y)\, u^2}{T^2}. \tag{18}$$

It corresponds to the irreversibility induced by Joule heating.

Total entropy generation

The total local entropy generation is therefore written as $S_{tot} = S_{th} + S_{vis} + S_{mag}$. The average total entropy generation over the computational domain is calculated as:

$$\overline{S}_{tot} = \frac{1}{V} \int_{0}^{V} S_{tot} \, dv. \tag{19}$$

3.5. The Bejan number

The Bejan number represents the relative contribution of thermal irreversibility to the total entropy generation; it is defined as the ratio of thermal entropy generation to the total entropy generation which includes thermal, viscous and magnetic contribution [46]:

$$Be = \frac{S_{th}}{S_{tot}}. \tag{20}$$

$Be \approx 1 \rightarrow$ thermal irreversibility dominates
$Be \approx 0 \rightarrow$ viscous/magnetic irreversibility dominates
The local Bejan number Be_{Local} is computed along the channel center line y_m to analyze the stream wise variation of the irreversibility. It is defined as the ratio of the local thermal entropy generation to the sum of thermal, viscous and magnetic entropy generation components.

$$Be_{Local} = \frac{S_{th}}{S_{tot}} = \frac{S_{th}}{S_{th} + S_{vis} + S_{mag}}. \tag{21}$$

The volume-averaged Bejan number is defined as the ratio of the volume-integrated thermal entropy generation to the volume-integrated total entropy generation, which includes thermal, viscous, and magnetic contributions.

$$\overline{Be} = \frac{\int_V S_{th} \, dv}{\int_V S_{tot} \, dv}. \tag{22}$$

4. Numerical Method

The governing equations were discretized and solved through the finite volume method in ANSYS Fluent. The SIMPLE algorithm. Patankar [47] was integrated into a pressure-based laminar solver to handle the flow field. Given the complexities of the MHD interactions, first-order upwind discretization was selected for all transport variables to ensure stability. The solution was considered converged once the residuals dropped below 10^{-6} for energy and 10^{-5} for both mass and momentum conservation.

4.1. Grid dependency

Grid independence was established by testing six mesh densities to ensure the stability of the solution. The cell count varied from 60000 to 204000, with Mesh m4 (142800 cells) being adopted for the final simulations. Table 4 presents the evolution of the average Nusselt number and maximum temperature across the tested grids, including the calculated relative errors. As shown in Figure 2, these key quantities converge consistently, confirming that Mesh m4 provides a grid-independent solution with high numerical accuracy.

It is observed that both quantities stabilize from the mesh containing 120400 cells onward. This indicates grid-independent solutions. Further mesh refinement does not lead to noticeable improvements, but the computational cost is significantly increased. Therefore, the mesh with 120400 cells m3 was selected for all subsequent simulations.

Table 4. Grid independence study for the average Nusselt number Nu_{avg} and maximum temperature T_{max}.

Mesh	Cells	Nu_{avg}	Error Nu_{avg}	T_{max} (K)	Error T_{max}
m1	60000	7.63337	0.07066	417.9590	0.04688
m2	93600	7.63301	0.06594	418.0190	0.03252
m3	120400	7.63008	0.02753	418.1387	0.00390
m4	142800	7.62798	–	418.1550	–
m5	176400	7.62661	0.01796	418.1560	0.00024
m6	204000	7.62668	0.01704	418.1603	0.00127

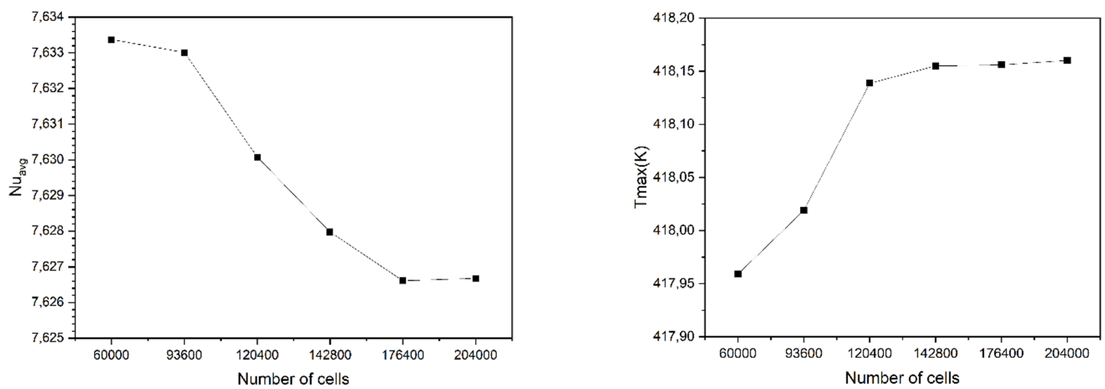

Figure 2. Effect of mesh refinement on Nu_{avg} and T_{max}.

4.2. Validations

To ensure the accuracy and reliability of the numerical model developed, validation was performed by comparing the numerical results obtained with previously published experimental data of Gohakhah et al. [48], and numerical of Mussan et al. [49]. Figure 3 illustrates the comparison of the average convective heat transfer coefficient h_{ave} as a function of the Reynolds number Re for two magnetic field intensities, $B = 0$ T and $B = 0.05$ T.

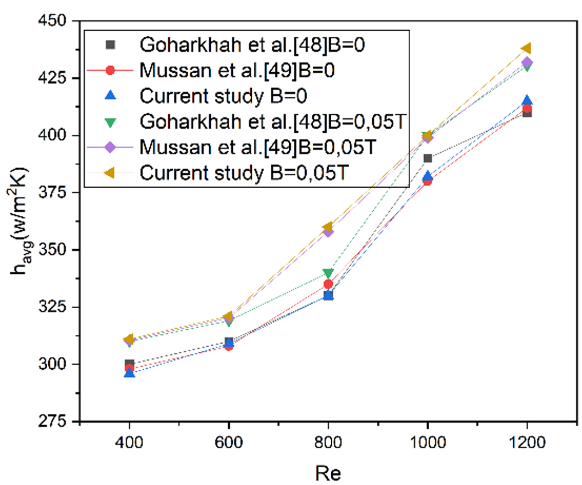

Figure 3. Cross validation of the developed model against the experimental study of Goharkhah et al. [48] and the numerical study of Mussan et al. [49].

The experimental data of Goharkhah et al. [48] and numerical of Mussan et al. [49], with a maximum discrepancy of less than 5% across the evaluated range of Re. The accuracy of the computational model and the numerical procedures and boundary conditions used is confirmed by this strong correlation.

5. Results and Discussions

This section presents a detailed analysis of the magnetohydrodynamic hybrid nanofluid flow in the smooth and wavy channels. The effects of Reynolds number and magnetic field intensity are investigated from hydrodynamic, thermal, and thermodynamic perspectives. The discussion first focuses on the flow structure and Lorentz force, followed by heat transfer and Joule heating characteristics. Finally, entropy generation and Bejan number analyses are presented to evaluate the distribution of irreversibility in the system.

In the present study, the magnetic field is spatially non-uniform and follow an exponential distribution $B = B_0 e^{-ky}$. Consequently, the Hartmann number $Ha(y)$ becomes position-dependent. To avoid introducing a spatially varying control parameter and to ensure clarity in the parametric analysis, the results are expressed in terms of the reference magnetic field strength B_0 corresponding to the maximum magnetic field. This approach allows for a more direct physical interpretation of the magnetic intensity's influence on the hybrid nanofluid flow. Simulations were conducted for an Fe_3O_4-Al_2O_3/water hybrid nanofluid (1% and 8% concentrations) across a Reynolds number range of $200 \leq Re \leq 800$. The study assumes a constant Rayleigh number of $Ra = 1.38 \times 10^5$ and a Prandtl number of 6.04, while exploring magnetic field strengths of $B_0 = 1, 2, 4$, and 8 T.

Figure 4 compares the axial velocity evolution along the channel center line for the wavy and smooth configurations at different Reynolds numbers. Upstream of the heated section, both configurations exhibit identical hydrodynamic behavior, indicating that the wall waviness does not affect the flow before the heated region. Once the flow enters the magnetized section, a sharp velocity drop is observed due to the Lorentz-force-induced magnetic damping. This reduction becomes more pronounced at higher Reynolds numbers. Inside the heated section, the wavy channel exhibits noticeable velocity oscillations caused by repeated flow acceleration and deceleration induced by wall undulations. Downstream of the magnetic region, the velocity progressively recovers as the Lorentz force vanishes.

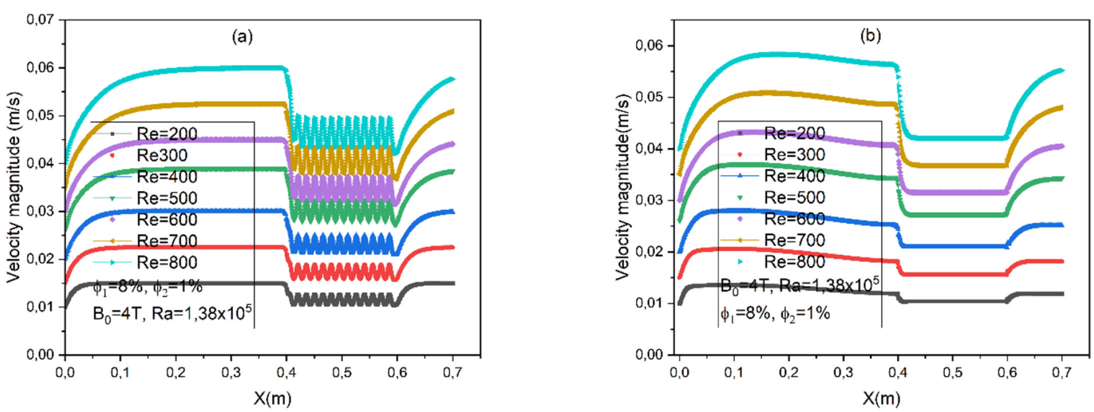

Figure 4. Axial velocity distribution along the channel centerline for different Reynolds numbers. (a) Wavy channel (WC); (b) Smooth channel (SC).

Figure 5 illustrates the effect of magnetic field intensity on the axial velocity for both channel configurations at a fixed Reynolds number. Upstream of the heated section, all velocity profiles collapse, confirming the absence of magnetic influence in this region. Once the flow enters the magnetized zone, a sharp velocity reduction is observed, which becomes more pronounced as the magnetic field intensity increases. This behavior is attributed to the Lorentz-force-induced magnetic damping that acts as an additional flow resistance. The velocity profiles become progressively flatter with increasing magnetic field strength, indicating flow stabilization. Compared with the smooth channel, the wavy channel exhibits local velocity oscillations due to repeated flow acceleration and deceleration induced by wall undulations.

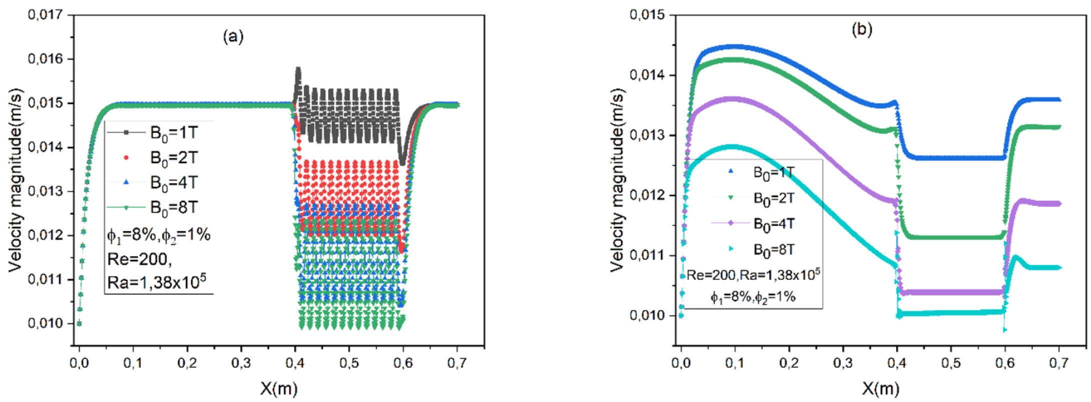

Figure 5. Axial velocity distribution along the channel center line for different magnetic field intensities at a fixed Reynolds number. (a) Wavy channel (WC); (b) Smooth channel (SC).

Figures 6 and 7 show the velocity contours for $Re = 500$ at two magnetic field intensities $B_0 = 1$ T and 4 T for both wavy WC (a) and smooth SC (b) channels.

At low magnetic field $B_0 = 1$ T (Figure 6), the wavy channel (a) exhibits strong spatial velocity modulation characterized by alternating acceleration and deceleration zones induced by periodic wall undulations. In contrast, the smooth channel (b) maintains a nearly parabolic velocity distribution with weak flow perturbation.

When the magnetic field increases to $B_0 = 4$ T in Figure 7, the magnetic field is applied in the heated and magnetized section of the channel. As the magnetic field strength increases, the Lorentz force damps the core flow and modifies the velocity distribution. The velocity gradients progressively shift toward the upper heated wall, where stronger thermal effects and buoyancy-driven acceleration enhance near-wall flow. In the wavy channel, the oscillatory velocity pattern is strongly attenuated, indicating that the magnetic field suppresses the hydrodynamic effects induced by wall waviness. This demonstrates the dominant stabilizing role of the Lorentz force at high magnetic field intensity.

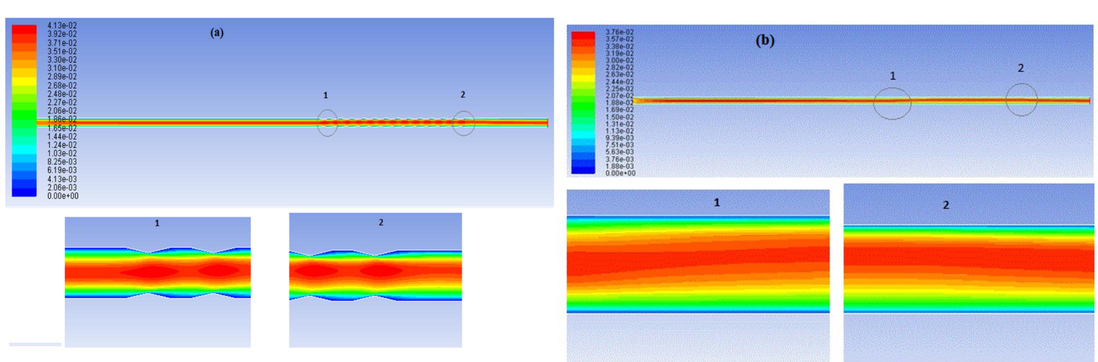

Figure 6. Velocity magnitude contours at $Re = 500$ for magnetic field intensity $B_0 = 1$ T: (a) wavy channel WC and (b) smooth channel SC.

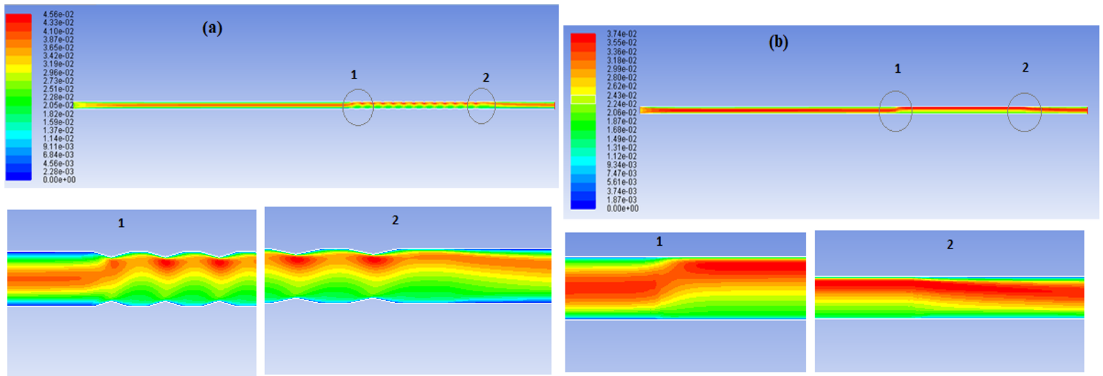

Figure 7. Velocity magnitude contours at $Re = 500$ for magnetic field intensity $B_0 = 4$ T: (a) wavy channel WC and (b) smooth channel SC.

To better understand the magnetic influence on the flow dynamics, the distribution of the Lorentz force is analyzed next. The Lorentz force is confined to the magnetized region of the channel.

Figure 8 illustrates the stream wise evolution of the Lorentz force for both channel configurations. The Lorentz force is presented as a volumetric body force (N/m^3) representing the electromagnetic resistance (Laplace force) acting within the magnetized region of the channel and opposing the flow. The Lorentz force appears only within the magnetized region and increases significantly with Reynolds number due to the increase in fluid velocity. The peak Lorentz force shifts slightly downstream as the Reynolds number increases, indicating deeper penetration of the high-speed core into the magnetic region.

A clear difference between the two channel configurations is observed. The smooth channel exhibits a single and smooth Lorentz force peak, whereas the wavy channel produces higher and spatially oscillating Lorentz force due to periodic acceleration and deceleration of the flow induced by wall undulations. This demonstrates the strong coupling between flow inertia and magnetic damping in the wavy configuration.

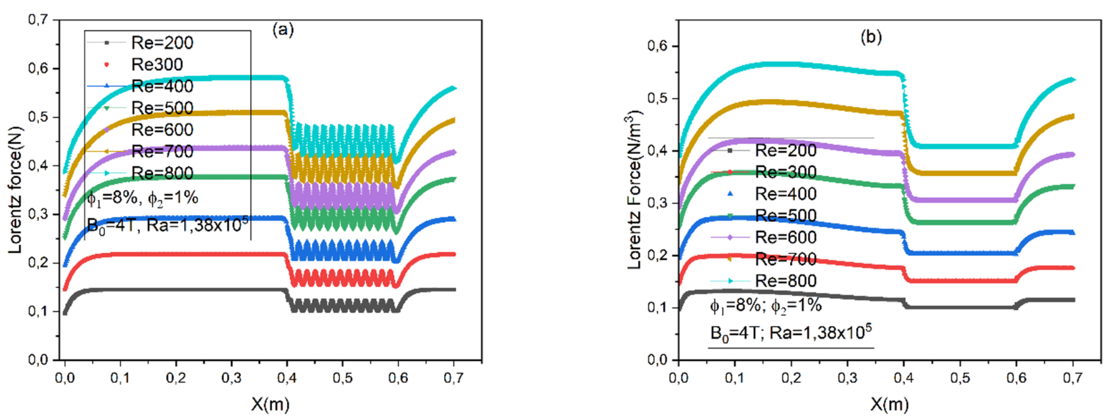

Figure 8. Variation of the Lorentz force along the channel center line for different Reynolds numbers at constant magnetic field intensity: (a) wavy channel (WC) and (b) smooth channel (SC).

Figure 9 shows the evolution of the Lorentz force for different magnetic field intensities. As expected, the Lorentz force increases significantly with magnetic field strength due to its quadratic dependence on the magnetic field. The peak Lorentz force becomes much larger and the affected region slightly widens as the magnetic field increases.

A marked difference between the two configurations is observed. The wavy channel exhibits stronger and spatially oscillating Lorentz force compared to the smooth channel because wall undulations induce local acceleration of the flow. These results highlight the strong coupling between magnetic damping and channel geometry.

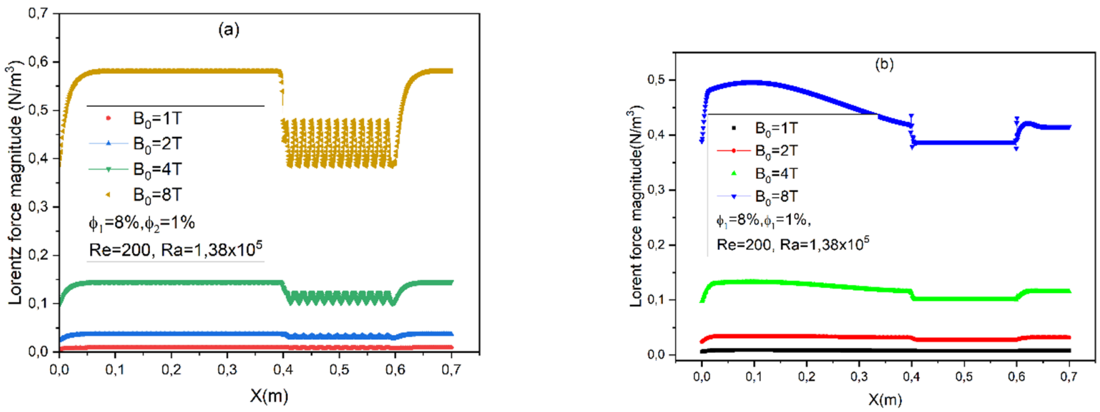

Figure 9. Variation of the Lorentz force along the channel center line length for different magnetic field intensities at fixed Reynolds number for the two channel configurations: (a) wavy channel (WC) and (b) smooth channel (SC).

To investigate the thermal response of the hybrid nanofluid to the applied magnetic field, temperature contours are presented for the wavy and smooth channel configurations at different magnetic field intensities. Figures 10 and 11 illustrate the temperature contours for two magnetic field intensities. Increasing the magnetic field from $B_0 = 1$ T to $B_0 = 4$ T significantly alters the thermal field. The fluid temperature rises and the thermal boundary layer becomes thicker due to reduced convective transport and enhanced Joule heating. The wavy channel exhibits a more pronounced temperature increase and stronger thermal mixing compared to the smooth channel. This behavior highlights the combined influence of magnetic damping and wall-induced mixing on the thermal performance of the system.

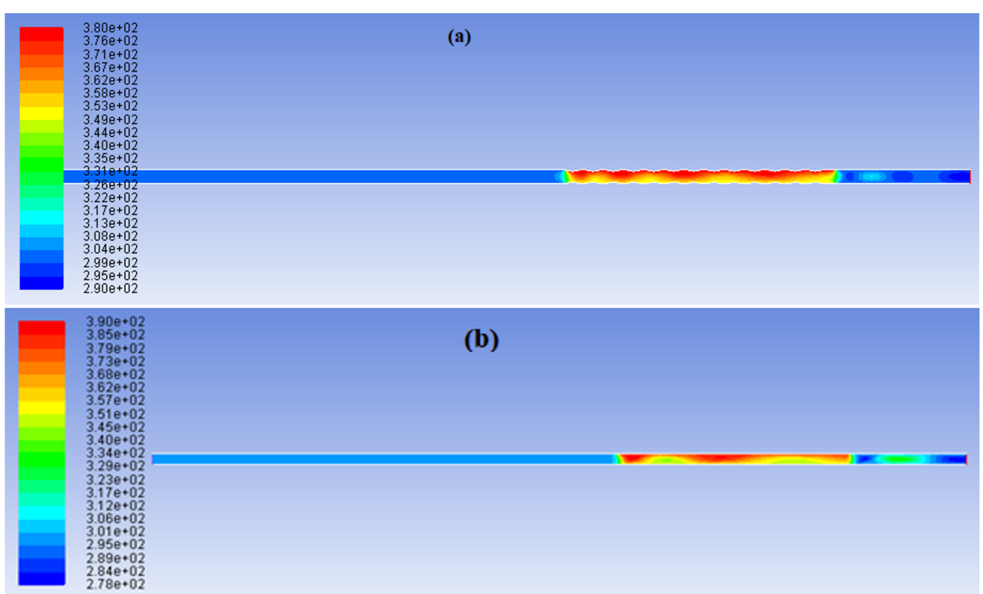

Figure 10. Temperature contours at $Re = 500$ and $B_0 = 1$ T for the two channel configurations: (a) wavy channel (WC) and (b) smooth channel (SC).

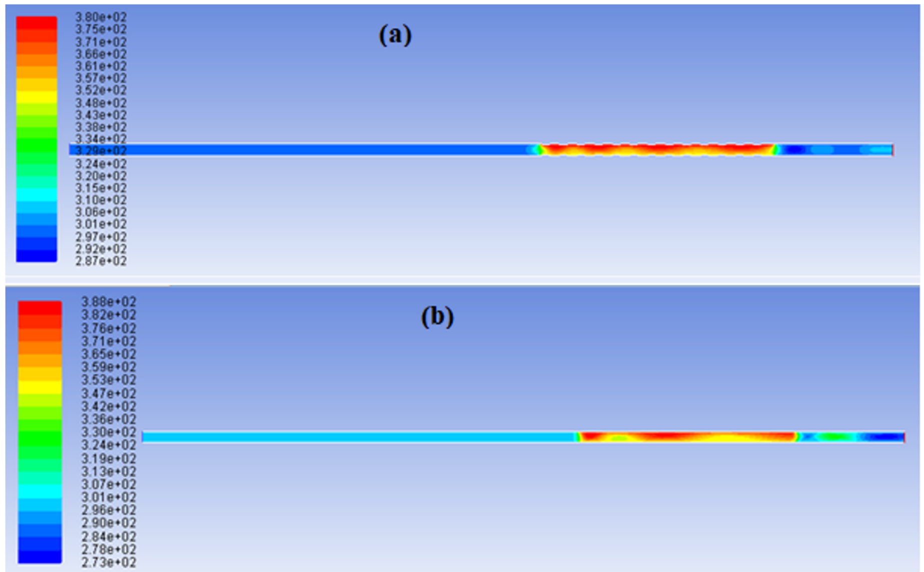

Figure 11. Temperature contours at $Re = 500$ and $B_0 = 4$ T for the two channel configurations: (a) wavy channel (WC) and (b) smooth channel (SC).

The magnetic heat generation induced by Joule heating is analyzed along the channel for different Reynolds numbers and magnetic field intensities.

Figures 12 and 13 present the distribution of magnetic joule heating along the channel. Joule heating appears only within the magnetized region and increases significantly with both Reynolds number and magnetic field intensity due to its quadratic dependence on velocity and magnetic field strength. The wavy channel produces significantly higher and spatially oscillating magnetic heat generation because wall undulations induce local velocity peaks and flow recirculation. The results confirm that the magnetic field acts as an internal heat source, explaining the temperature increase observed in the thermal contours and represents a major source of irreversibility in the system. It is clearly observed that the magnetic heat generation in the wavy channel is significantly higher than in the smooth channel. This behavior is attributed to the local acceleration and recirculation induced by wall undulations, which increase the fluid velocity and consequently enhance Joule heating. Overall, the wavy configuration produces greater magnetic heat generation than the smooth channel, highlighting the strong coupling between wall geometry and electromagnetic dissipation.

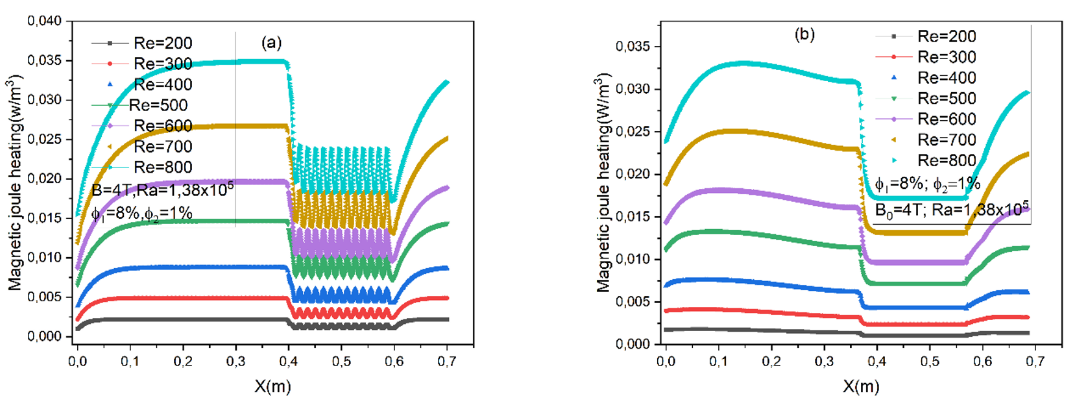

Figure 12. Streamwise evolution of the magnetic joule heating for different Reynolds numbers at constant magnetic field intensity: (a) wavy channel (WC) and (b) smooth channel (SC).

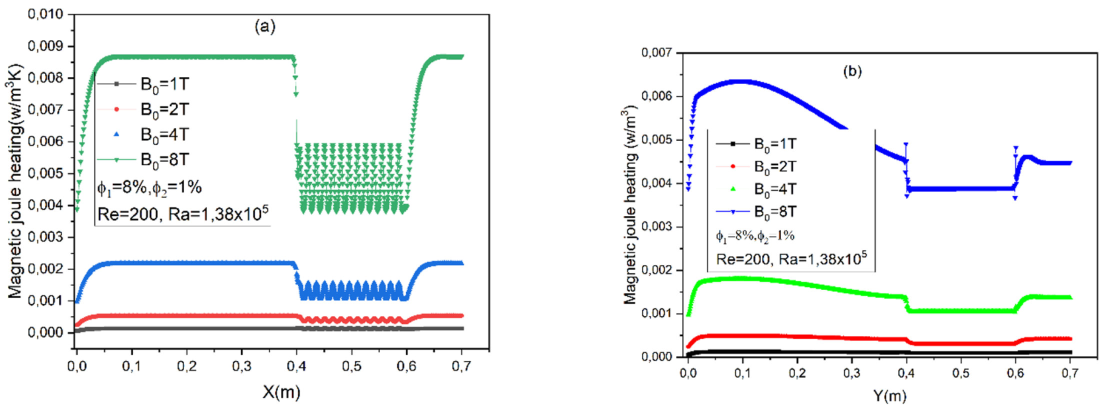

Figure 13. Streamwise evolution of the magnetic joule heating for different magnetic field intensities at fixed Reynolds number: (a) wavy channel (WC) and (b) smooth channel (SC).

To assess the thermodynamic irreversibility's of the system, entropy generation is examined for the hybrid nanofluid flow in both channel configurations. The total entropy generation consists of contributions from heat transfer, viscous dissipation, and magnetic effects associated with Joule heating and Lorentz forces.

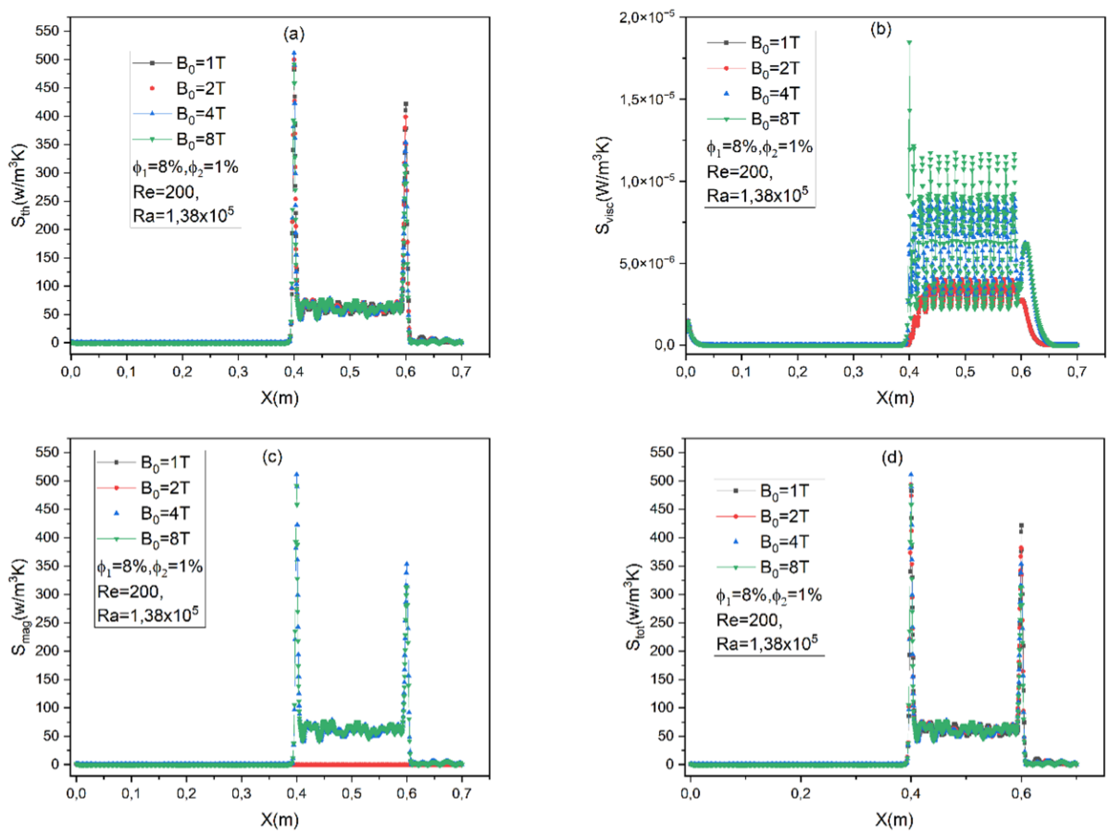

Figure 14. Streamwise distribution of entropy generation components for different magnetic field intensities at constant Reynolds number: (a) thermal entropy generation S_{th}, (b) viscous entropy generation S_{vis}, (c) magnetic entropy generation S_{mag}, and (d) total entropy generation S_{tot} for the wavy channel (WC).

Increasing the magnetic field intensity significantly enhances thermal and magnetic entropy generation, while viscous entropy slightly decreases due to magnetic damping of the flow. At high magnetic field intensity, magnetic entropy becomes the dominant source of irreversibility. The wavy channel consistently exhibits higher entropy generation than the smooth channel, highlighting the strong influence of wall geometry on thermodynamic losses.

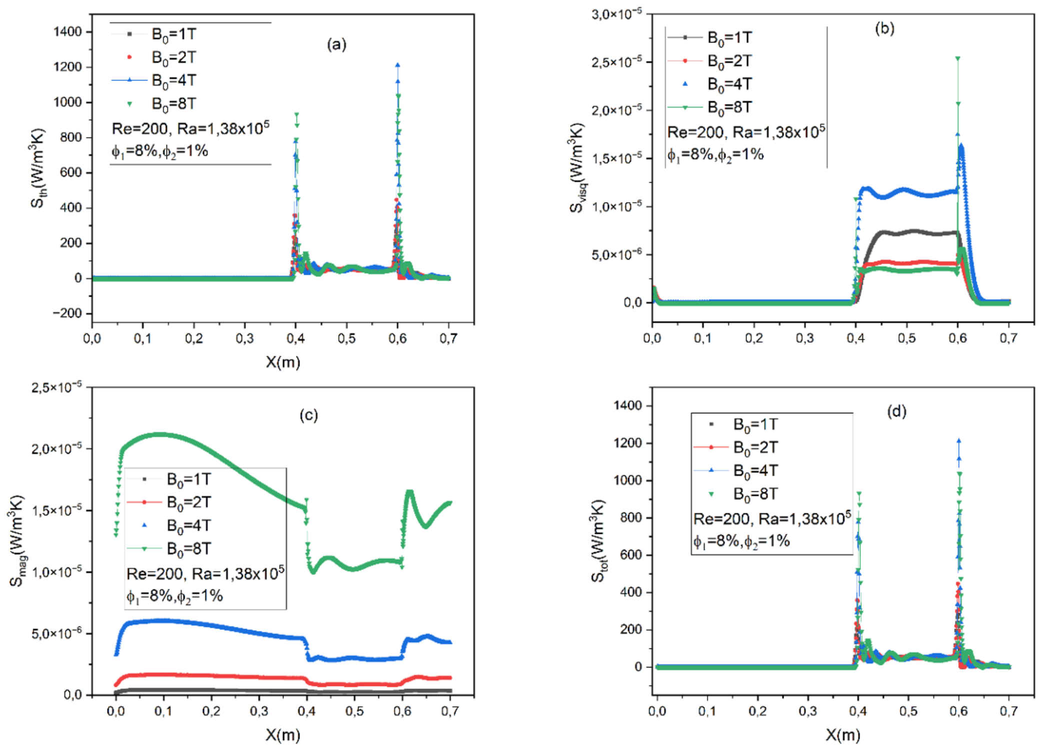

Figure 15. Streamwise distribution of entropy generation components for different magnetic field intensities at constant Reynolds number: (a) thermal entropy generation S_{th}, (b) viscous entropy generation S_{vis}, (c) magnetic entropy generation S_{mag}, and (d) total entropy generation S_{tot} for the smooth channel (SC).

In the smooth channel, thermal entropy generation is weakly influenced by Reynolds number under strong magnetic field conditions, as magnetic damping reduces convective effects. Viscous entropy slightly increases with Reynolds number due to enhanced velocity gradients. However, magnetic entropy generation exhibits a strong quadratic dependence on Reynolds number and becomes the dominant source of irreversibility. Consequently, total entropy generation is primarily governed by magnetic effects at high Reynolds numbers (Figure 17).

In the wavy channel, entropy generation increases more significantly with Reynolds number compared to the smooth configuration. Wall undulations enhance velocity gradients and local acceleration, which intensify thermal, viscous, and magnetic entropy generation. Although magnetic entropy remains dominant at high Reynolds numbers, viscous contributions become more pronounced due to geometric effects. This demonstrates that wall waviness amplifies thermodynamic irreversibility's under strong magnetic field conditions.

To further evaluate the global thermodynamic performance of the system, the volume-averaged total entropy generation is analyzed for both channel configuration as function of the magnetic field intensity and Reynolds number.

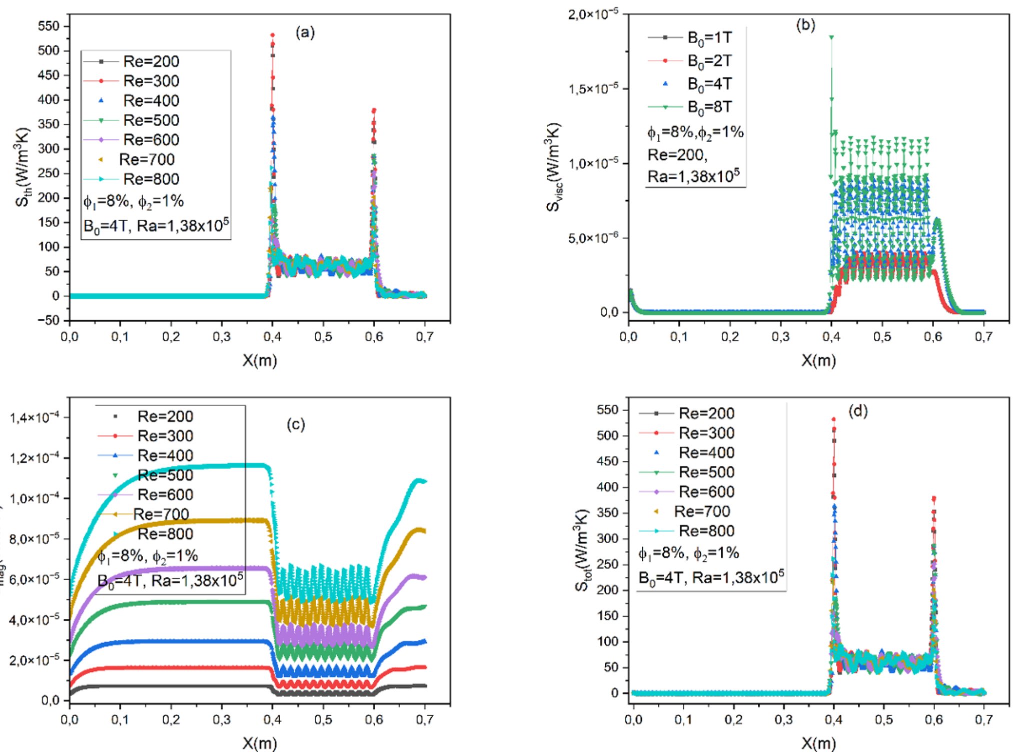

Figure 16. Streamwise distribution of entropy generation components for different Reynolds number at constant reference magnetic intensity B_0: (a) thermal entropy generation S_{th}, (b) viscous entropy generation S_{vis}, (c) magnetic entropy generation S_{mag}, and (d) total entropy generation S_{tot} for the wavy channel (WC).

Figure 18 illustrates the variation of the volume averaged total entropy generation for smooth and wavy channels. The results provide insight into the overall irreversibility's in the system and allow a direct comparison of the thermodynamic performance of the two geometrical configuration.

Figure 18(a) illustrates the variation of the volume-averaged total entropy generation with magnetic field intensity for smooth and wavy channel configurations. The smooth channel exhibits a significant increase in total entropy generation as magnetic field intensity increases. In contrast, the wavy channel maintains nearly constant entropy generation due to enhanced fluid mixing induced by wall undulations. Consequently, the wavy channel configuration reduces global thermodynamic irreversibility compared with the smooth channel.

Figure 18(b) presents the variation of the volume-averaged total entropy generation with Reynolds number for both channel configurations. For smooth channel, entropy generation increases significantly with Reynolds number due to higher velocity gradients and enhanced electromagnetic dissipation. In contrast, the wavy channel exhibits lower entropy generation over the entire Reynolds number range. The wall undulations improve fluid mixing and thermal distribution, which reduces global thermodynamic irreversibility's. As a result, the wavy configuration demonstrates superior thermodynamic performance compared to the smooth channel.

These results confirm that the channel geometry plays a crucial role in controlling thermodynamic irreversibility in magneto hydrodynamic nano hybrid flows.

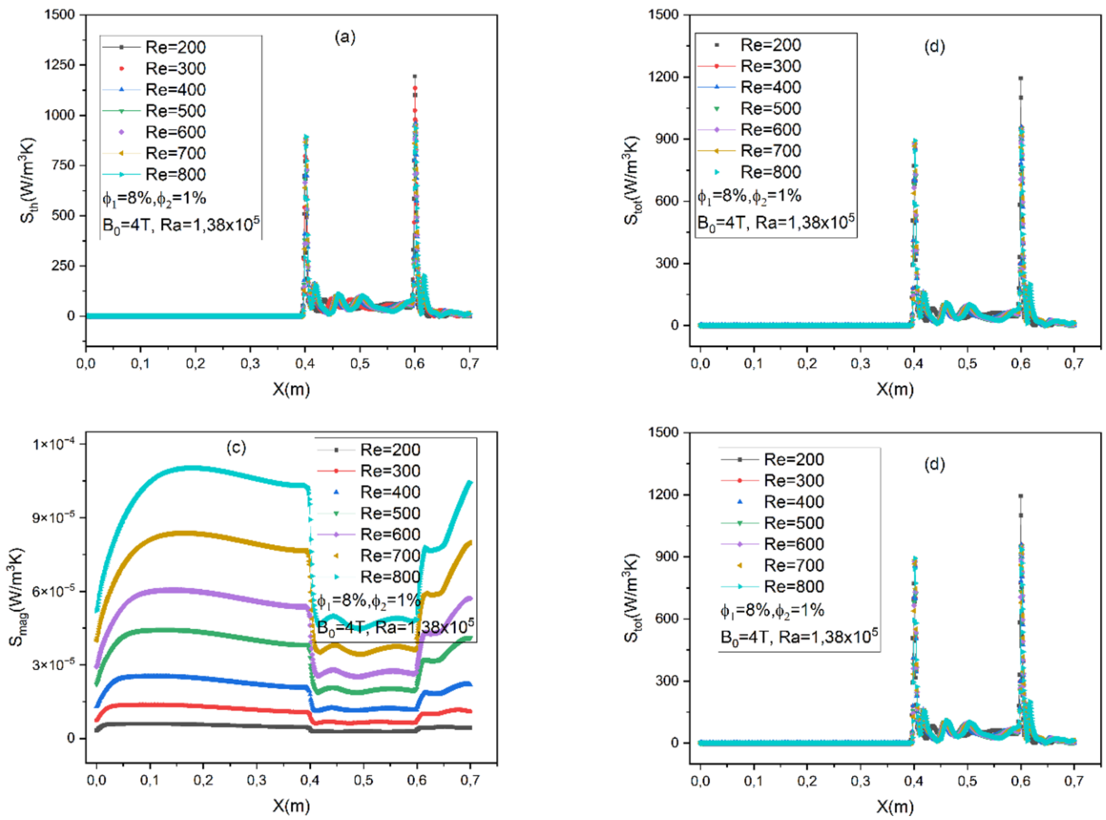

Figure 17. Streamwise distribution of entropy generation components for different Reynolds number at constant reference magnetic intensity B_0: (a) thermal entropy generation S_{th}, (b) viscous entropy generation S_{vis}, (c) magnetic entropy generation S_{mag}, and (d) total entropy generation S_{tot} for the smooth channel (SC).

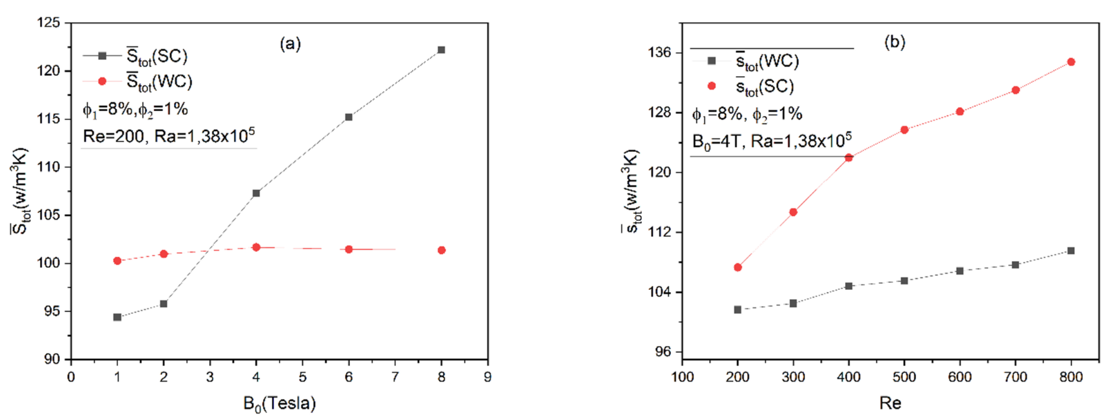

Figure 18. Variation of the volume-averaged total entropy generation for the wavy (WC) and smooth (SC) channel configuration: (a) as function of the magnetic field intensity B_0 and (b) as function of the Reynolds number.

To further asses the heat transfer performance of the system, the variation of the average Nusselt number is examined for both channel configuration as function of the Reynolds number and the magnetic field intensity.

Figure 19(a) presents the variation of the average Nusselt number as function of the magnetic field intensity B_0. The results indicate that the average Nusselt number decreases with increasing magnetic field intensity for both channel configurations. This behavior is mainly due to the action of the Lorentz force, which acts as a resistive force opposing the fluid motion. The magnetic field suppresses the flow velocity, reduces convective transport, and consequently weakens heat transfer.

Figure 19(b) presents the variation of the average Nusselt number as function of the Reynolds number. From this figure it can be observed that the average Nusselt number increases with increasing Reynolds number for the two configurations. This behavior is attributed to the enhancement of the convective heat transfer as the flow velocity increases. Higher Reynolds numbers leads to stronger fluid motion and a thinner thermal boundary layer, which promotes heat transfer between the heated walls and the fluid. Furthermore, the wavy channel consistently exhibits higher Nusselt numbers than the smooth channel. The presence of wall undulations disturbs the flow and enhances the fluid mixing, which intensifies the heat transfer process. Consequently, the wavy geometry improves the thermal performance of the system compared to the smooth configuration. These results are consistent with the entropy generation analysis, where the (WC) exhibits lower overall thermodynamic irreversibility while maintaining higher heat transfer rates. Therefore, the (WC) geometry provides a more efficient thermal configuration by enhancing heat transfer while reducing entropy generation.

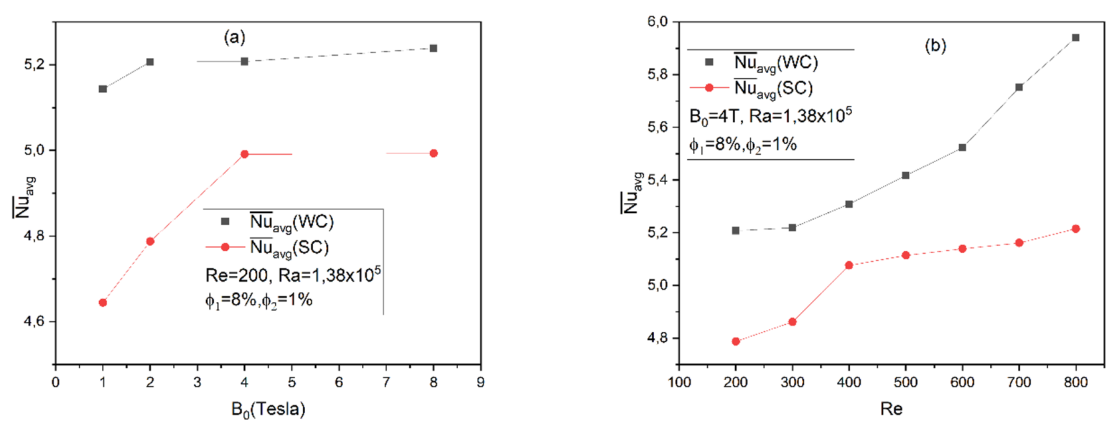

Figure 19. Variation of the average Nusselt number for the wavy (WC) and smooth (SC) channel configuration: (a) as function of the magnetic field intensity B_0 and (b) as function of the Reynolds number Re.

To provide a comprehensive assessment of the systems performance, it is essential to bridge the gap between heat transfer enhancement and thermodynamic efficiency. While the Nusselt number characterizes the cooling effectiveness, the entropy generation analysis identifies the sources of energy degradation. In this section, the local Bejan number Be_{Local} is discussed to elucidate the impact of the wavy wall geometry the non-uniform magnetic field and the Reynolds number on the flow irreversibility.

Figure 20 shows the variation of the local Bejan number for different magnetic field intensities for wavy and smooth channels. Figure 20(a) presents the variation of the local Bejan number for the wavy channel configuration (WC). It is observed from this figure that the local Bejan number distribution reveals a clear transition in the source of irreversibility along the channel. In the entry region ($x < 0.4$), sharp decline in Be are observed, reaching value close to zero. This indicates that in the absence of significant thermal gradients, entropy generation is purely driven by fluid friction (viscous dissipation). As the fluid enters the active zone ($0.4 \leq x \leq 0.6$), the Bejan number rises sharply to unity ($Be \approx 1$). This shift confirms that the intense thermal exchange imposed by the heated walls (380 K and 350 K) becomes the primary source of entropy production, overshadowing both viscous and magnetic dissipation. The fact that $Be \approx 1$ suggests that the configuration is optimized for heat transfer, as the majority of energy loss is utilized for thermal exchange rather being wasted through fluid friction or joule heating. Figure 20(b) for the smooth configuration (SC). It is seen from this figure that the smooth channel configuration (SC) exhibit a distinct behavior compared to the wavy channel (WC). The Be_{Local} profile clearly delineate the different physical regimes along the channel. In the initial unheated section ($x < 0.4$), Be_{Local} drops towards zero, indicating that the entropy generation is exclusively governed by viscous dissipation as thermal gradients are negligible. Upon entering the active zone ($0.4 \leq x \leq 0.6$), a sharp transition to $Be \approx 1$ is observed. This signifies that the thermal irreversibility, triggered by the substantial temperature difference between the heated walls and the hybrid nanofluid becomes dominant mechanism.

In Figure 21(a) and (b), the local Bejan number distribution along the channel are presented for both wavy and smooth configurations at different Reynolds numbers. In the wavy configuration (WC), significant oscillations of the Bejan number appear within the heated and corrugated region due to periodic acceleration and deceleration of the flow. As the Reynolds number increases, the Bejan number decreases, indicating a growing contribution of viscous and magnetic irreversibility. In contrast, the smooth channel exhibit higher Bejan numbers with weaker oscillations, suggesting that the thermal entropy generation remains dominant in most of the flow domain.

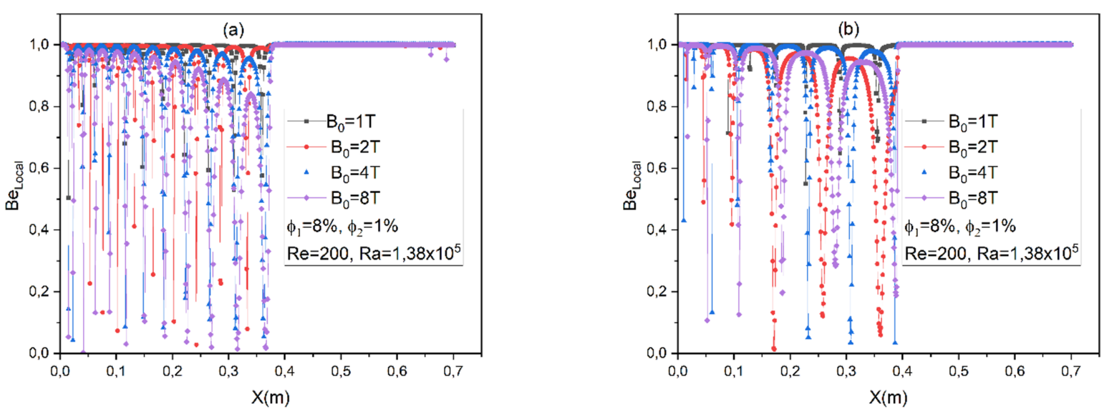

Figure 20. Streamwise distribution of the local Bejan number for different magnetic intensity B_0 for: (a) the wavy channel (WC) and (b) the smooth channel (SC).

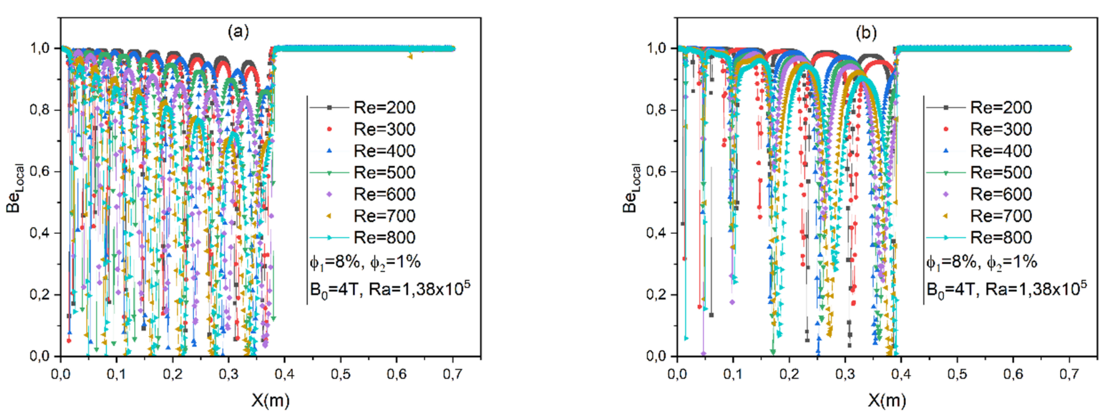

Figure 21. Streamwise distribution of the local Bejan number for different Reynolds number for: (a) the wavy channel (WC) and (b) the smooth channel (SC).

Table 5 summarizes the variation of the volume-averaged thermal entropy generation S_{th}, the total entropy generation S_{tot}, and the corresponding Bejan number Be for the both wavy channel (WC) and smooth channel (SC) under magnetic field intensities B_0 and Reynolds number Re. It is first observed that the values of S_{th} and S_{tot} remain very close for investigated conditions, resulting in Bejan number approaching unity ($Be \approx 1$). This is clearly indicating that the total entropy generation within the system is predominantly governed by thermal irreversibility, while the contribution associated with viscous dissipation and magnetic effects remain relatively small. Such behavior is typical of laminar forced convection flows where temperature gradients represent the main source of thermodynamic irreversibility. The effect of the magnetic field intensity B_0 reveals a gradual increase in both thermal and total entropy generation for the two channel configurations. This trend can be attributed to the action of the Lorentz force, which modifies the velocity distribution inside the channel and consequently alters temperature field.

Furthermore, a comparison between the two geometrical configurations shows that the smooth channel consistently produces higher generation than the wavy channel. This observation suggests that the wavy geometry improves the thermodynamic performance of the system by reducing global irreversibility. The presence of wall undulations promotes better mixing of the fluid and leads to a more uniform temperature distribution, which mitigates excessive thermal gradients and consequently reduce entropy production.

Table 5. Comparison of the volume-averaged thermal entropy generation $\bar{S}_{th}$, total entropy generation $\bar{S}_{tot}$ and Bejan number for the wavy channel (WC) and smooth channel (SC) at different magnetic field intensities B_0 and Reynolds numbers Re.

Waved channel (WC)				**Smooth channel (SC)**			
B_0	$\bar{S}_{th}$ **(W/m^{3}wk)**	$\bar{S}_{tot}$ **(W/m^{3}wk)**	$\overline{Be}$	B_0	$\bar{S}_{th}$ **(W/m^{3}wk)**	$\bar{S}_{tot}$ **(W/m^{3}wk)**	$\overline{Be}$
1	100,26436	100,26437	1	1	94,38623	94,38639	1
2	100,97951	100,97952	1	2	95,76666	95,76766	1
4	101,66123	101,66139	1	4	107,26107	107,26152	1
8	101,45502	101,45530	1	8	122,19570	122,19600	1
Re				**Re**			
200	101,66123	101,66139	1	200	107,26107	107,26152	1
300	102,49719	102,49756	1	300	114,71110	114,71111	1
400	104,78584	104,78650	0,99999	400	121,98490	121,98545	1
500	105,54110	105,54221	0,99999	500	125,71832	125,72095	0,99998
600	102,87041	102,87190	0,99999	600	128,13222	128,13566	0,99997
700	102,66793	102,66995	0,99998	700	130,99945	131,00101	0,99999
800	104,51922	104,52186	0,99997	800	134,79035	134,79238	0,99998

6. Conclusion

In this study, the hydrodynamic, thermal, and thermodynamic behavior of a hybrid nanofluid flowing in smooth and wavy channel configurations under the influence of a localized non-uniform magnetic field was numerically investigated. The effect of the Reynolds number and magnetic field intensity on the velocity field, Lorentz force, Joule heating, entropy generation and heat transfer performance were analyzed.

The results showed that the presence of a magnetic field significantly alters the flow structure through the action of the Lorentz force, which acts as a resistive force opposing the fluid motion. As the magnetic field intensity increases, the velocity within the magnetized region decreases and the flow becomes more stable. At the same time, Joule heating increases due to the electromagnetic interaction, leading to a rise in the fluid temperature and modification of thermal boundary layer. The entropy generation analysis revealed that thermal entropy generation remains the dominant source of irreversibility in the system, as confirmed by Bejan numbers close to unity. Although magnetic entropy generation increases with magnetic field intensity and Reynolds number, its contribution remains smaller with thermal irreversibility.

A comparison between the two channel configurations demonstrated that the wavy channel significantly modifies the flow dynamics through periodic acceleration and deceleration of the fluid. This geometry modulation enhances fluid mixing and improves heat transfer, resulting in higher Nusselt numbers compare with the smooth channel.

From a thermodynamic perspective, the wavy channel generally exhibits lower volume averaged-entropy generation than the smooth channel, indicating reduced global thermodynamic irreversibility. Consequently, the wavy configuration provides a better compromise between heat transfer enhancement and thermodynamic efficiency.

Overall, the present results highlight the important role of channel geometry in controlling heat transfer and entropy generation in magneto hydrodynamic hybrid nanofluid flows. The use of wavy channel configuration can therefore represent an effective strategy for improving the thermal performance of MHD cooling systems and energy-related applications.

Funding: This research received no external funding.

Author contributions: Conceptualization, S.B.; Methodology, S.A.; Software, S.B.; Validation, B.M.; Formal Analysis, S.A.; Investigation, S.A.; Resources, S.B.; Data Curation, B.M.; Writing – Original Draft Preparation, S.B.; Writing– Review & Editing, S.A. and B.M.; Visualization, B.M.; Supervision, S.A.; Project Administration, F.Q.; Funding Acquisition, R.A.

Disclosure statement: The authors declare no conflict of interest.

Nomenclature

B_0	Magnetic field (Tesla)
C_p	Specific heat (J/kg·K)
D_h	Hydraulic diameter (m)
g	Gravitational acceleration (m/s^2)
$h(x)$	Local heat transfer coefficient (W/m^{2}K)
k_f, k_s	Fluid and solid thermal conductivities (W/mK)
P	Pressure (N/m^2)
$q(x)$	Local heat flux (W)
S	Entropy generation (W/m^{3}K)
T	Temperature (K)
u, v	Velocity components in x and y directions (m/s)
WC, SC	Waved and smooth channel
x, y	Cartesian coordinates (m)
α	Thermal diffusivity (m^2/s)
β	Thermal expansion coefficient (1/K)
φ	Solid volume concentration
μ	Dynamic viscosity (Pa·s)
ν	Kinematic viscosity (m^2/s)
ρ	Density (kg/m^3)
σ	Electrical conductivity (S/m)

Subscripts

bf	Base fluid
c	Cold
f	Fluid
h	Hot
hnf	Hybrid nanofluid
avg	Average
o	Reference
th	Thermal
tot	Total
vis	Viscous
w	Wall

References

[1] B. Mohamad. Improving heat transfer performance of flat plate water solar collectors using nanofluids. *Journal of Harbin Institute of Technology (New Series)*, 32(2):80–89, 2025.

[2] S. Benkherbache and M. Si-Ameur. Numerical solution on mixed convection flow of nanofluid around a finned angular sector of heat sink. *Computational Thermal Sciences: An International Journal*, 15(3), 2023.

[3] W. Ashraf. Heat transfer mechanism in ternary nanofluid between parallel plates channel using modified Hamilton-Crossers model and thermal radiation effects. *Geoenergy Science and Engineering*, 225:211732, 2023.

[4] F. F. Qader, B. Mohamad, A. M. Hussein, and S. H. Danook. Numerical study of heat transfer in circular pipe filled with porous medium. *Pollack Periodica*, 19(1):137–142, 2024.

[5] F. Selimefendigil and H. F. Öztop. MHD pulsating forced convection of nanofluid over parallel plates with blocks in a channel. *International Journal of Mechanical Sciences*, 157:726–740, 2019.

[6] M. Sheikholeslami and D. Ganji. Heat transfer of Cu-water nanofluid flow between parallel plates. *Powder Technology*, 235:873–879, 2013.

[7] S. Suresh, K. P. Venkitaraj, P. Selvakumar, and M. Chandrasekar. Synthesis of Al_2O_3–Cu/water hybrid nanofluids using two step method and its thermo physical properties. *Colloids and Surfaces A: Physicochemical and Engineering Aspects*, 388(1–3):41–48, 2011.

[8] M. Arshad, A. Hassan, Q. Haider, F. M. Alharbi, N. Alsubaie, A. Alhushaybari, D.-P. Burduhos-Nergis, and A. M. Galal. Rotating hybrid nanofluid flow with chemical reaction and thermal radiation between parallel plates. *Nanomaterials*, 12(23):4177, 2022.

[9] H. Xu. Mixed convective flow of a hybrid nanofluid between two parallel inclined plates under wall-slip condition. *Applied Mathematics and Mechanics*, 43(1):113–126, 2022.

[10] N. C. Roy and I. Pop. Analytical investigation of transient free convection and heat transfer of a hybrid nanofluid between two vertical parallel plates. *Physics of Fluids*, 34(7), 2022.

[11] J. Sarkar, P. Ghosh, and A. Adil. A review on hybrid nanofluids: recent research, development and applications. *Renewable and Sustainable Energy Reviews*, 43:164–177, 2015.

[12] G. Huminic and A. Huminic. Hybrid nanofluids for heat transfer applications – a state-of-the-art review. *International Journal of Heat and Mass Transfer*, 125:82–103, 2018.

[13] A. Shaheen, M. Imran, H. Waqas, M. Raza, and S. Rashid. Thermal transport analysis of squeezing hybrid nanofluid flow between two parallel plates. *Advances in Mechanical Engineering*, 15(1), 2023.

[14] S. Benkherbache, S. Amroune, A. Belaadi, S. Zergane, and C. Farsi. Numerical analysis of natural convection in an annular cavity filled with hybrid nanofluids under magnetic field. *Energies*, 17(18):4671, 2024.

[15] I. Waini, A. Ishak, and I. Pop. Unsteady flow and heat transfer past a stretching/shrinking sheet in a hybrid nanofluid. *International Journal of Heat and Mass Transfer*, 136:288–297, 2019.

[16] N. M. Albqmi and S. Sivanandam. Entropy generation and thermal radiation impact on magneto-convective flow of heat-generating hybrid nano-liquid in a non-Darcy porous medium with non-uniform heat flux. *Computation*, 12(3):43, 2024.

[17] K. Ali, S. Ahmad, K. S. Nisar, A. A. Faridi, and M. Ashraf. Simulation analysis of MHD hybrid Cu-Al_2O_3/H_2O nanofluid flow with heat generation through a porous media. *International Journal of Energy Research*, 45(13):19165–19179, 2021.

[18] T. E. Tayari, L. Torkzadeh, D. Ganji, and K. Nouri. Investigating the MHD flow of hybrid nanofluid Al_2O_3-CuO with brownian motion between two parallel plates using RBF. *International Journal of Thermofluids*, page 101458, 2025.

[19] S. Hosseinzadeh and D. D. Ganji. A novel approach for assessment of MHD mixed fluid around two parallel plates by consideration hybrid nanoparticles and shape factor. *Alexandria Engineering Journal*, 61(12):9779–9793, 2022.

[20] T. Anwar, A. Khan, S. A. Abas, M. Fiza, H. Ullah, and S. M. Al-Mekhlafi. Bio-convective magnetized ternary hybrid nanofluid flow between two parallel plates: A numerical approach. *International Journal of Thermofluids*, 29:101392, 2025.

[21] A. Ali, M. Ahmed, A. Ahmad, and R. Nawaz. Enhanced heat transfer analysis of hybrid nanofluid over a Riga plate: incorporating Lorentz forces and entropy generation. *Tribology International*, 188:108844, 2023.

[22] S. Murtaza, N. Becheikh, A. U. Rahman, A. Sambas, C. Maatki, L. Kolsi, and Z. Ahmad. Thermal performance analysis of a nonlinear couple stress ternary hybrid nanofluid in a channel: A fractal–fractional approach. *Nanomaterials*, 14(22):1855, 2024.

[23] G. Kalpana, K. Madhura, and R. B. Kudenatti. Magnetohydrodynamic boundary layer flow of hybrid nanofluid with the thermophoresis and brownian motion in an irregular channel: A numerical approach. *Engineering Science and Technology, an International Journal*, 32:101075, 2022.

[24] A. Chattopadhyay, R. Malo, H. F. Öztop, S. K. Pandit, and K. D. Goswami. Simulation of magneto mixed convective flow and thermal behavior of hybrid nanofluid in a partially heated wavy cavity. *Journal of Magnetism and Magnetic Materials*, 575:170713, 2023.

[25] J. I. Ahad, A. Hossain, A. Parvin, and M. M. Molla. Magnetohydrodynamics thermosolutal convection of hybrid MWCNT-Fe_3O_4-water nanofluid along a vertical wavy surface with wall heat and mass flux. *Partial Differential Equations in Applied Mathematics*, 10:100667, 2024.

[26] I. Haider, N. Jabeen, A. Hussain, A. Smerat, N. Ben Khedher, and Y. M. Riyad. Laminar turbulent transition in magnetohydrodynamic hybrid nanofluid flow with eddy, joule heating, brownian motion and mass based stream line flow over wedged surface with slips effects. *Aerospace Science and Technology*, page 111130, 2025.

[27] Y. Ma, R. Mohebbi, M. M. Rashidi, and Z. Yang. MHD convective heat transfer of Ag-MgO/water hybrid nanofluid in a channel with active heaters and coolers. *International Journal of Heat and Mass Transfer*, 137:714–726, 2019.

[28] S. Khatun, R. Kundu, S. Islam, R. Aktary, and D. Kumar. Sensitivity analysis on natural convective trapezoidal cavity containing hybrid nanofluid with magnetic effect: Numerical and statistical approach. *Heliyon*, 11(1):e41508, 2025.

[29] S. A. Abdollahi, A. Alizadeh, I. C. Esfahani, M. Zarinfar, and P. Pasha. Investigating heat transfer and fluid flow betwixt parallel surfaces under the influence of hybrid nanofluid suction and injection with numerical analytical technique. *Alexandria Engineering Journal*, 70:423–439, 2023.

[30] L. Tlau and S. Ontela. Entropy generation in MHD nanofluid flow with heat source/sink. *SN Applied Sciences*, 1(12):1672, 2019.

[31] N. Parveen, M. Awais, S. E. Awan, W. U. Khan, Y. He, and M. Y. Malik. Entropy generation analysis and radiated heat transfer in MHD (Al_2O_3-Cu/Water) hybrid nanofluid flow. *Micromachines*, 12(8):887, 2021.

[32] I. Ahmad, Q. Zan-Ul-Abadin, M. Faisal, K. Loganathan, T. Javed, and S. Gyeltshen. Entropy analysis in bidirectional hybrid nanofluid containing nanospheres with variable thermal activity. *Journal of Nanomaterials*, page 1915185, 2022.

[33] A. Tahiri, H. Ragueb, M. Moussaoui, K. Mansouri, D. Guerraiche, and K. Guerraiche. Heat transfer and entropy generation in viscous-Joule heating MHD microchannels flow under asymmetric heating. *International Journal for Numerical Methods in Heat & Fluid Flow*, 34(10):3953–3978, 2024.

[34] S. Nadeem, B. Ishtiaq, J. Alzabut, and H. A. Ghazwani. Entropy generation for exact irreversibility analysis in the MHD channel flow of Williamson fluid with combined convective-radiative boundary conditions. *Heliyon*, 10(4):e26432, 2024.

[35] S. Jena and M. Mishra. Entropy analysis of Cu-Al_2O_3 based hybrid and Cu based mono nanofluid flows through porous medium: A comparative study. *Case Studies in Thermal Engineering*, 50:103463, 2023.

[36] S. Hussain, S. E. Ahmed, and T. Akbar. Entropy generation analysis in MHD mixed convection of hybrid nanofluid in an open cavity with a horizontal channel containing an adiabatic obstacle. *International Journal of Heat and Mass Transfer*, 114:1054–1066, 2017.

[37] A. Abdulkadhim, K. Al-Chlaihawi, F. Al-Daamee, and H. K. Hamzah. Numerical investigation of MHD double-diffusive flow and entropy generation in a corrugated enclosure with a star-shaped inner body. *International Communications in Heat and Mass Transfer*, 169:109853, 2025.

[38] S. Bilal, N. Z. Khan, K. Pan, and T. Salahuddin. Heat transfer augmentation and entropy generation minimization by employing synergistic aspects of hybrid (Fe_3O_4 + MWNTs) nanoliquid in star shaped enclosure with thermally conductive cylinder and inclined magnetic field aspects. *Journal of Molecular Liquids*, 401:124728, 2024.

[39] M. Mehrali, E. Sadeghinezhad, A. R. Akhiani, S. Tahan Latibari, H. S. C. Metselaar, A. S. Kherbeet, et al. Heat transfer and entropy generation analysis of hybrid graphene/Fe_3O_4 ferro-nanofluid flow under the influence of a magnetic field. *Powder Technology*, 308:149–157, 2017.

[40] F. Mabood, A. Shafiq, W. A. Khan, and I. A. Badruddin. MHD and nonlinear thermal radiation effects on hybrid nanofluid past a wedge with heat source and entropy generation. *International Journal for Numerical Methods in Heat & Fluid Flow*, 32(1):120–137, 2022.

[41] K. Rafique, Z. Mahmood, Adnan, U. Khan, T. Muhammad, A. Mir, W. Aich, and L. Kolsi. Unsteady MHD flow analysis of hybrid nanofluid over a shrinking surface with porous media and heat generation: Computational study on entropy generation and Bejan number. *International Journal of Heat and Fluid Flow*, 107:109419, 2024.

[42] E. J. Ndelwa, M. H. Mkwizu, A. X. Matofali, and A. O. Ali. Entropy analysis of MHD hybrid nanofluid in a rotating channel filled with porous material. *International Journal of Thermofluids*, 24:100887, 2024.

[43] D. Sáchica, C. Treviño, and L. Martínez-Suástegui. Numerical study of magnetohydrodynamic mixed convection and entropy generation of Al_2O_3-water nanofluid in a channel with two facing cavities with discrete heating. *International Journal of Heat and Fluid Flow*, 86:108713, 2020.

[44] M. Sheikholeslami, M. Gorji-Bandpy, and D. Ganji. Numerical investigation of MHD effects on Al_2O_3–water nanofluid flow and heat transfer in a semi-annulus enclosure using LBM. *Energy*, 60:501–510, 2013.

[45] M. A. Mansour, S. Siddiqa, R. S. R. Gorla, and A. Rashad. Effects of heat source and sink on entropy generation and MHD natural convection of Al_2O_3-Cu/water hybrid nanofluid filled with square porous cavity. *Thermal Science and Engineering Progress*, 6:57–71, 2017.

[46] A. Bejan. *Entropy Generation through Heat and Fluid Flow*. John Wiley & Sons, New York, 1982.

[47] S. Patankar. *Numerical Heat Transfer and Fluid Flow*. CRC Press, 2018.

[48] M. Goharkhah, A. Salarian, M. Ashjaee, and M. Shahabadi. Convective heat transfer characteristics of magnetite nanofluid under the influence of constant and alternating magnetic field. *Powder Technology*, 274:258–267, 2015.

[49] M. A. Mohsin, R. Kareem, R. S. Tofah, and S. R. Nfawa. Numerical investigation of ferrohydrodynamic magnetic nanofluid convection in a trapezoidal cavity channel. *Case Studies in Thermal Engineering*, 75:107066, 2025.